6

Hybrid seismic imaging

M. Mendes, J.-L. Mari, M. Hayet

Traditionally, each seismic prospection technique requires the optimization of field layout, equipment and configuration dependent on the target, attempting to record only the proposed seismic wave, with the highest possible quality. Although setup parameters are designed specifically for selected wave types, seismic records are always corrupted by other waves. To isolate a single wave type, data processing methods are applied for the extraction and/or minimization of all other arrivals.

Conversely, this chapter addresses how it is possible to take advantage of several existing wave types, within the same dataset, encouraging the application of hybrid seismic methods. The objective being to obtain a final model that is built with the information produced by different seismic processing sequences, which thus improves significantly the delineation of seismic velocity interfaces and/or the physical parameterization of subsurface geological structures. Thus, the proposed hybrid seismic strategy offers economic and practical benefits because its implementation can be carried out without increasing the costs of seismic data acquisition, while data processing follows standard procedures.

Here, we focus on two field examples that target shallow structures, the final results of which emphasize the advantage of applying hybrid seismic methods to provide more accurate geophysical models.

The first example presents a refraction-reflection imaging strategy with the capability to evaluate reflectivity information from the acquisition surface. Depending on the minimum offset defined for the survey, standard reflection imaging techniques usually start to image the reflectivity parameter a few meters below the surface, therefore refracted arrivals are used to complete the reflectivity features for the shallowest structures.

The procedure involves three steps:

- construction of a depth velocity model from first arrival times, accomplished iteratively by tomographic inversion,
- construction of a time reflectivity section from the reflected waves of direct and reverse shot gathers by classical reflection seismic processing. Generally, this is the most critical step in the imaging procedure, due to the low fold of reflection data,
- extension up to the surface of the time reflectivity section by converting the shallowest depth velocity model to time reflectivity, associated with velocity contrasts in the subsurface. The time reflectivity sections require a factor scale before being gathered in a final time reflectivity section.

As this hybrid approach has the capability to start imaging from the surface, it is a very useful tool for providing reflectivity information for targets located in the near and/or very near surface, which is often required for the monitoring of civil engineering structures, in environmental engineering studies and even archaeological exploration.

The second example described in this chapter relates to another hybrid seismic strategy for refraction-surface waves imaging. When a compressional wave source is used in surface seismic surveys, more than two-thirds of the total seismic energy generated is usually imparted into Rayleigh waves, the principal component of ground roll. This hybrid seismic technique addresses this issue by combining information about the P-wave velocity provided by the refraction arrivals with the S-wave velocity distribution obtained from the surface wave data, also presented on the same field records.

The velocity-estimation procedures include the following steps:

- construction of a P-wave velocity model from first arrival times accomplished iteratively by tomographic inversion. A large range of initial models are used to estimate the sensitivity and depth of the investigation. The final P-wave velocity model is an average of all models satisfying the picked field data within a predetermined fitting level;
- construction of an S-wave velocity model from the analysis of surface waves in the frequency-phase velocity domain. After field data windowing for the validation of a 1D model hypothesis; the experimental dispersion curve is easily identified in the f-k domain and the location of maxima energy can be picked.

By taking advantage of multi-shot acquisition setups, a stacked dispersion curve can be obtained. The dispersion curve is a diagram of phase velocity versus frequency. S-wave velocity can be obtained by the inversion of dispersion curves, using a global search method with a neighborhood algorithm (NA).

The distribution of both velocities is productively combined to evaluate mechanical properties of the subsurface, which are critical properties for many geotechnical foundation designs, aquifer system characterizations and the time-lapse monitoring of shallow water content.

6.1 Refraction-reflection imaging

The main purpose of this example is to obtain a complete shallow subsurface image for the reflectivity property through the simple and fast processing of refraction survey data.

The refraction survey was carried out near the underground research laboratory of Andra (National Radioactive Waste Management Agency) located in the eastern region of France. The refraction survey, collected by the geophysical company DMT GmbH & Co KG, aimed to estimate the velocity field in the near surface zone (weathering zone) for a reliable evaluation of static corrections. The intention was to improve the processing of a high-resolution 3D seismic survey of 37 km^2, which also covered this region (Figure 6.1).
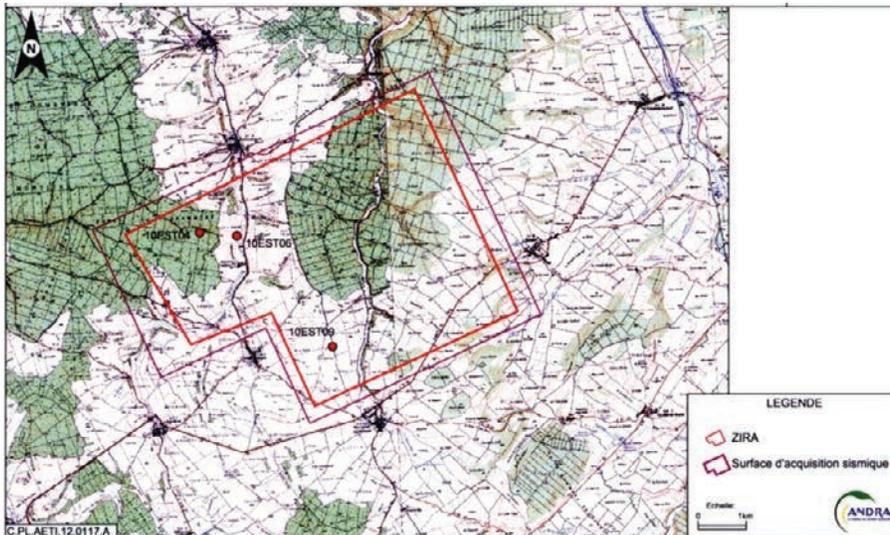

Figure 6.1 *Plan view of the 3D seismic reflection survey area (magenta polygon) with the location of three relevant 2D seismic refraction profiles (red points): 10EST04, 10EST09, 10EST06. Adapted from Mendes* et al. *(2014).*

Several refraction profiles were then implemented with a total spread length of 203 m for each profile. The 10 Hz vertical geophones, 48 in total, were spread with a receiver spacing of 2.5 m for source offsets ranging from 1 to 7.5 m and 5 m for source offsets larger than 7.5 m. The source was a weight dropper (10 kJ) shooting at 3 points: shot point 1 (SP01) with a 1 m offset from geophone 1, shot point 2 (SP02) with a 1 m offset from both geophones 24 and 25, and shot point 3 (SP03) with a 1 m offset from geophone 48. Figure 6.2 shows a diagram of the acquisition spread and the three common shot-gathers of the 10EST04 profile.
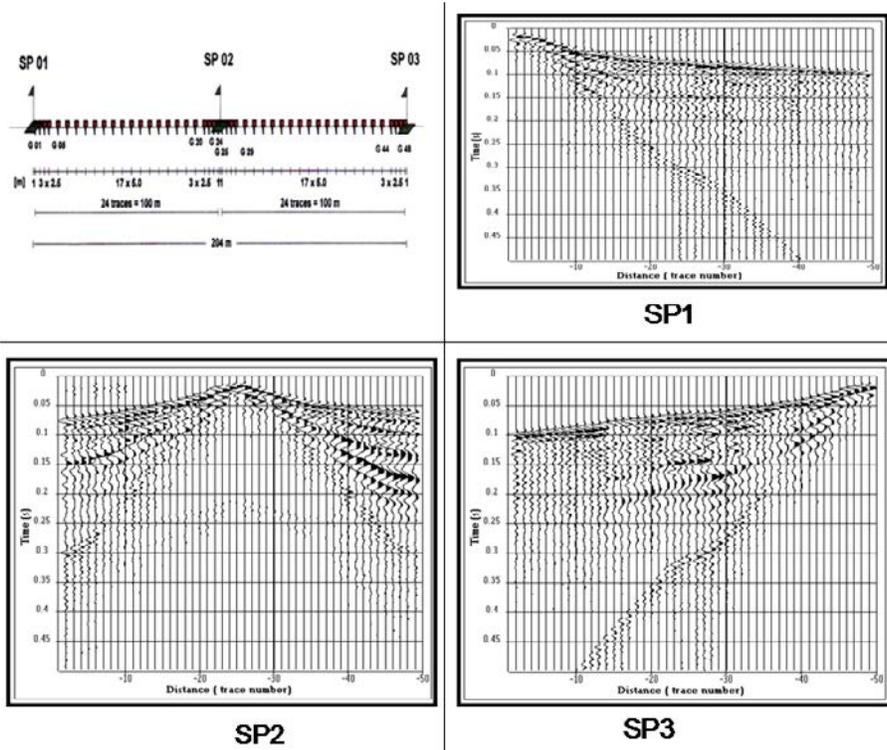

Figure 6.2 *Refraction seismic acquisition: spread and the three-common shot-gathers of the 10EST04 profile. Adapted from Mendes* et al. *(2014).*

Full details describing the acquisition and seismic hybrid processing of this field example are presented in Mendes, Mari and Hayet, 2014 (Mendes *et al.*, 2014). This chapter presents only a brief outline.

The first step was to derive a depth velocity model for the shallowest region from the processing of first arrivals (direct, diving or refracted waves). The Plus-Minus method of refraction interpretation (Hagedoorn, 1959) using the first-arrival time information was used to produce an interval velocity depth model: the weathered

layer presents constant velocity V1 = 1,300 m/s over a bedrock with velocity V2 = 3,250 m/s. This model, along with all available information, was then used to generate the best initial model for tomographic inversion. Tomography was applied to refine the velocity-depth model, which has major benefits when dealing with complex geological setups involving lateral variations. Figure 6.3 shows the advantages of processing by tomographic inversion where strong lateral velocity variations add value to the model. The weathering zone is a heterogeneous shaly mudstone over a compacted limestone.
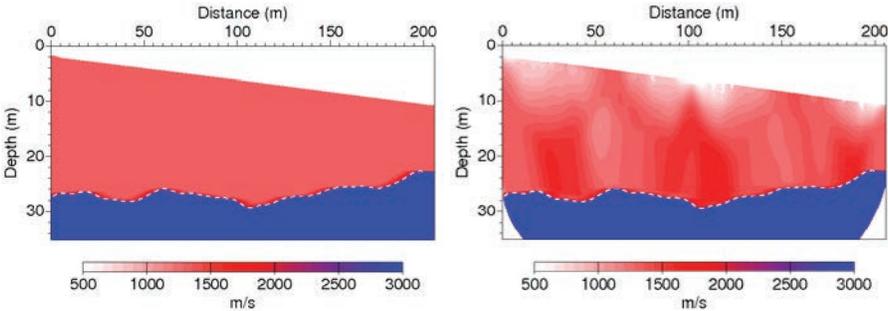

Figure 6.3 *Tomographic inversion for the 10EST04 profile. Left: Input model V1 = 1,300 m/s and V2 = 3,250 m/s provided by the Plus-Minus method. Right: Velocity model generated by tomographic inversion. The result exhibits velocity with strong lateral variations for the heterogeneous shaly mudstone over a bedrock of compact limestone. Adapted from Mendes* et al. *(2014).*

In a second step, only the reflection events were considered for imaging. In this case, processing capable of isolating and enhancing the reflected waves was required, since they derive from data recorded for a refraction survey and the shot-gathers were corrupted by energetic surface waves that arrived simultaneously with the reflected waves.

To obtain a single-fold reflectivity section, shot points 1 and 3 (the end-off shots) were processed according to the following standard sequence:

- amplitude recovery;
- deconvolution by spectrum equalization (12–160 Hz frequency bandwidth);
- wave separation by SVD extraction of refracted waves;
- wave separation by F-K filter, to extract surface waves and convert refracted waves;
- static corrections based on the high-resolution velocity model provided by the tomographic inversion;
- CMP sorting, traces gathered in a common shot-gather are sorted in a common midpoint-gather;

- velocity analysis by velocity scan to produce a velocity model;
- normal move-out (NMO) corrections to flatten the reflected arrivals.

Figure 6.4 illustrates the main evolution of field data during the processing sequence. Special attention was focused on the residual section (Figure 6.4-bottom right), which clearly shows high apparent velocity events associated with reflected waves.
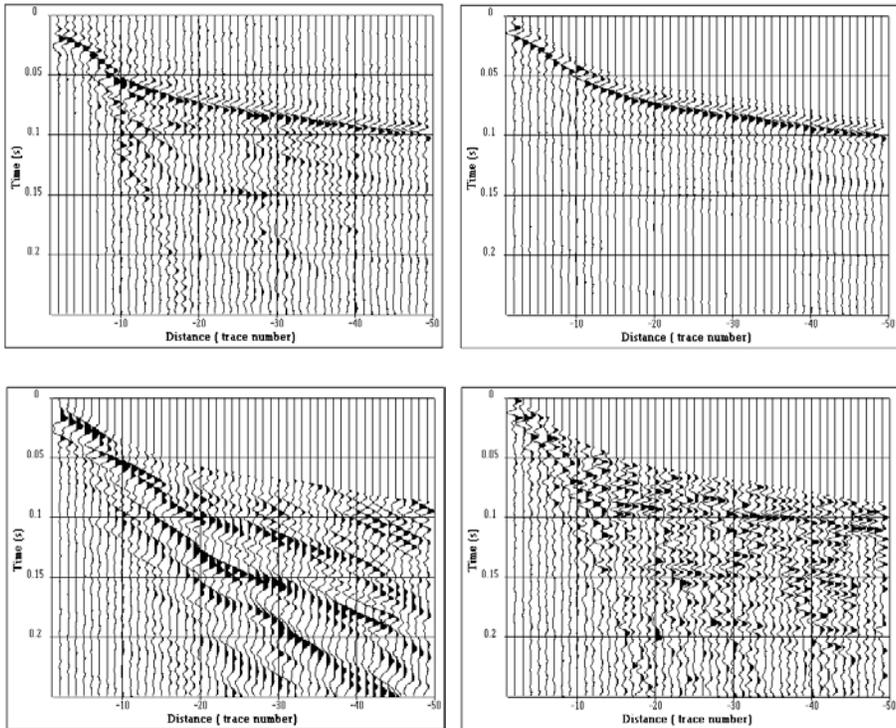

Figure 6.4 *Deconvolution and wave separation for shot point 1 of the 10EST04 profile. Top left: deconvolution by spectrum equalization in the 12–160 Hz frequency bandwidth. Top right: Extraction of direct and refracted waves by SVD filter. Bottom left: Extraction of surface waves (Pseudo Rayleigh waves) by F-K filter. Bottom right: Reflected waves and residual noise. Adapted from Mendes* et al. *(2014).*

Chapter 4 contains more information about the processing sequence, which readers should look through to gain further insight into the method.

The NMO correction produced a single fold section (Figure 6.5 left). We considered the traditional definition for reflectivity, $RZ_i = (Z_{i+1} - Z_i) / (Z_{i+1} + Z_i)$ where Z_i is the acoustic impedance (product of the density by velocity) at cell i and Z_{i+1} is the acoustic impedance at cell i+1. Nevertheless, density was neglected in our reflectivity

coefficient computation. Thus, this reflectivity section displays the reflection coefficients associated to the interfaces, filtered in the seismic frequency bandwidth.

The third and last step of this hybrid approach focuses on extending the reflectivity section upwards through the depth velocity model of the uppermost region, obtained by tomographic inversion. The depth velocity model was converted to time and used to estimate the reflectivity according the definition of $RV_i = (V_{i+1} - V_i)/(V_{i+1} + V_i)$ where V_i is the velocity at cell i and V_{i+1} is the velocity at cell i+1. The section obtained was then filtered in the same frequency bandwidth as defined for the section in the previous processing step.

Before they could be gathered into a single time reflectivity section, the two time reflectivity sections required a scale factor (k): the reflectivity section derived from the velocity model (RV) is related to the reflectivity section derived from acoustic impedance contrasts (RZ) by the equation RZ = kRV. The scale factor was computed by the amplitude ratio between the reflectivity sections in a time-distance window, where the reflected wave on the bottom of the weathering zone is visible. In practice, the time-distance window is defined as follows: time window (between 0.025 s and 0.050 s) for the short offsets (between 0 m and 25 m). Figure 6.5-bottom right shows the final time reflectivity section obtained by gathering the two reflectivity sections also shown in Figure 6.5, where a noticeable reflection at approximately 40 ms is associated with the bottom of the weathering zone.
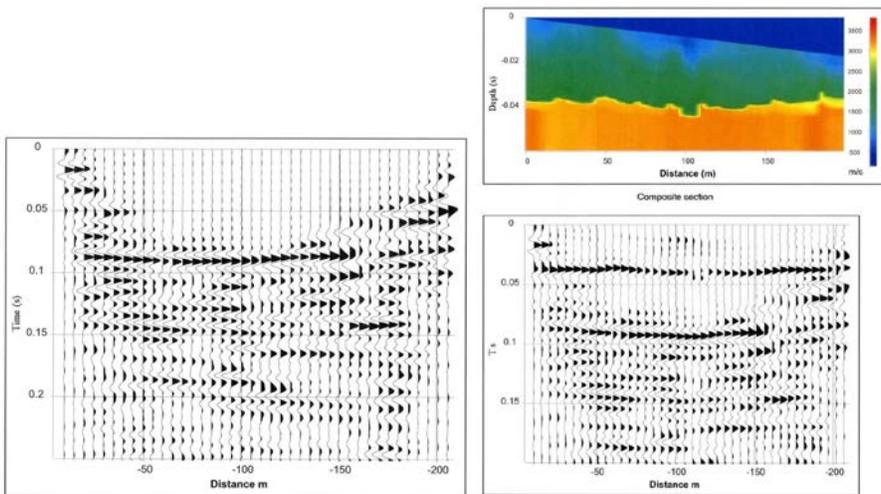

Figure 6.5 *Reflectivity section for 10EST04 profile: Left: Single fold section derived from reflection processing of off-end shots. Bottom right: Upward continuation of single-fold section using reflectivity derived from tomographic velocity model. Top right: Time converted velocity model obtained by tomographic inversion. Adapted from Mendes* et al. *(2014).*

The field data examples illustrate the potential of gathering two sections, extracted from different parts of the seismic wave field, for providing a means to resolve reflectivity and images from the ultra-shallow surface down to deeper structures. This is achieved using a simple seismic data processing method, with data acquired in a rapid and inexpensive manner, for refraction seismic surveying, without increasing the acquisition costs.

6.2 Refraction-surface waves imaging

The main objective of this example is to encourage the processing of P-wave refraction and surface-wave data obtained from a single seismic survey.

The geophysical survey was carried out in Yellowstone National Park (USA), in the Obsidian Pool Thermal Area. The goal of the seismic survey carried out at this site was to study shallow hydrothermal systems, characterize fluid pathways and improve understanding of the depths at which steam separates from liquid water. The area is characterized by extensive CO_2 diffuse degassing and isolated thermal features with water temperatures between 21.9 °C and 84.0 °C. Seismic data were collected in July 2016 along a south-southwest–north-northeast transect, crossing a heat-flow anomaly between 50 and 120 m and a degassing feature between 86 and 96 m.

The equipment and parameters used in the seismic survey were:

- a 5.4 kg sledgehammer source swung onto a metal plate. The plate was hit five times at each position to increase the S/N,
- 10 Geometrics Geode seismographs, with 24-channels in each one,
- 4.5 Hz vertical component geophones spaced every 1 m, obtaining a 239 m long profile,
- 25 shot gathers recorded every 10 m,
- a sampling rate of 0.125 ms and a recording time of 0.75 s, to include the full surface wavefield.

In addition, a GPS survey and airborne LiDAR data collection were carried out to extract the topography.

The following results are extracted from Pasquet and Bodet (2017), who have developed an open-source MATLAB-based package that performs surface wave inversion and profiling (SWIP) to obtain 1D to 2D variations of S-wave velocity.

The first step of the proposed velocity-estimation procedure concerns the P-wave velocity model.

The construction of the P-wave velocity model from the first arrival times was accomplished iteratively by tomographic inversion. A large range of 100 initial models were tested to estimate the sensitivity and depth of investigation. The final P-wave velocity model produced is an average of all models satisfying the picked

field data within a predetermined fitting level; it shows smoothly varying velocities ranging between 100 and 2,000 m/s, with a low velocity layer, approximately 5 m thick, at the surface.

Figure 6.6 shows the layout of the seismic acquisition setup, with 240 geophones and 25 shots, the shot-gather for a source located at 120 m and the final P-wave velocity model obtained from P-wave travel time tomography.
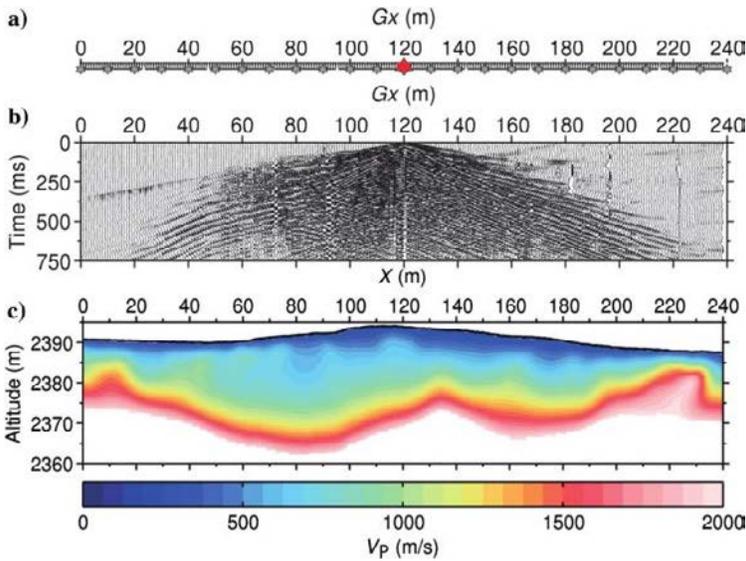

Figure 6.6 (a) Layout of the seismic acquisition setup, with 240 geophones (gray triangles) spaced every 1 m and 25 shots (gray stars) spaced every 10 m. (b) Example of a shot gather for a source located at 120 m (red star in a). (c) Final P-wave velocity model obtained from P-wave travel time tomography. The topography extracted from airborne LiDAR data is represented with a solid black line. From Pasquet and Bodet (2017).

The second step of the velocity-estimation procedure is related to the S-wave velocity model extracted from the surface waves. The processing of the surface waves data was carried out using SWIP and readers can find supplementary information about this practical processing sequence in Pasquet and Bodet (2017). Therefore, very few details are provided here and we restrict our comments to the main results only.

After field data windowing for validation of the 1D model hypothesis, the seismic record from its original time–distance domain was transformed into the frequency–phase-velocity domain. This step results in a set of frequency–phase-velocity pairs specifying dispersion curves. The experimental dispersion curves were identified in the f-k domain and the location of maxima energy were picked. The dispersion

curve is a diagram of phase velocity versus frequency and Figure 6.7 shows examples of single dispersion curves from shots located at 0 m, 10 m, 50 m, and 60 m.
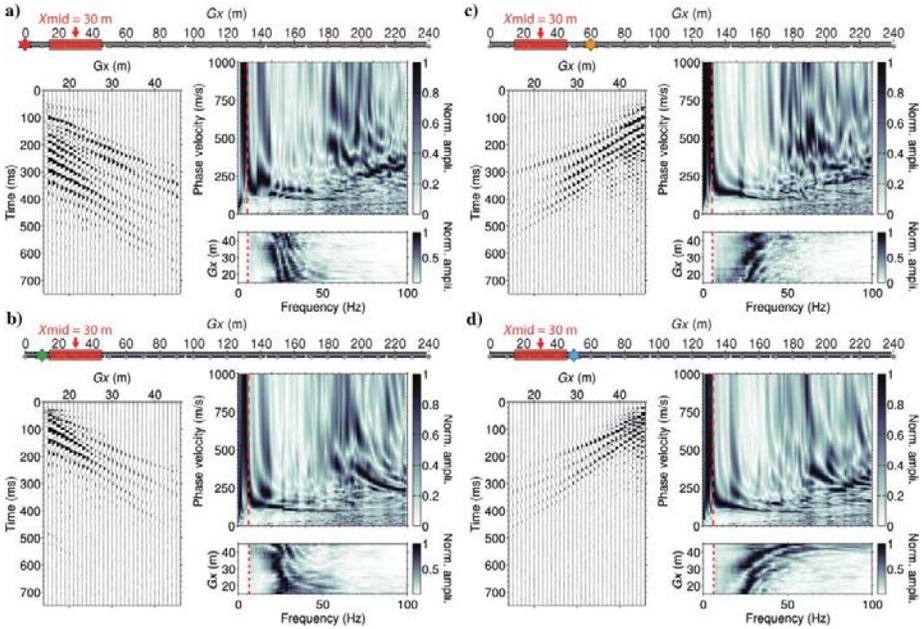

Figure 6.7 *Extraction of single dispersion images for a 31 trace window centered at Xmid=30 m, using shots located at (a) 0 m, (b) 10 m, (c) 50 m, and (d) 60 m. On each inset, windowed shot gathers are on the left, corresponding spectrograms are at the bottom right, and computed dispersion images are at the top right. The dashed red lines on the spectrograms and dispersion images correspond to automatic low-cut frequencies defined from the spectrogram amplitude. From Pasquet and Bodet (2017).*

Through the utilization of multi-shot acquisition setups, a stacked dispersion curve can be obtained, and the S/N ratio improved, as shown in Figure 6.8.

The dispersive events were stacked on the frequency–phase velocity panel, and then the interactive picking of events was conducted. Figure 6.8 presents two examples of stacked dispersion curves with picked events for the fundamental and first modes. The associated uncertainties are also defined.
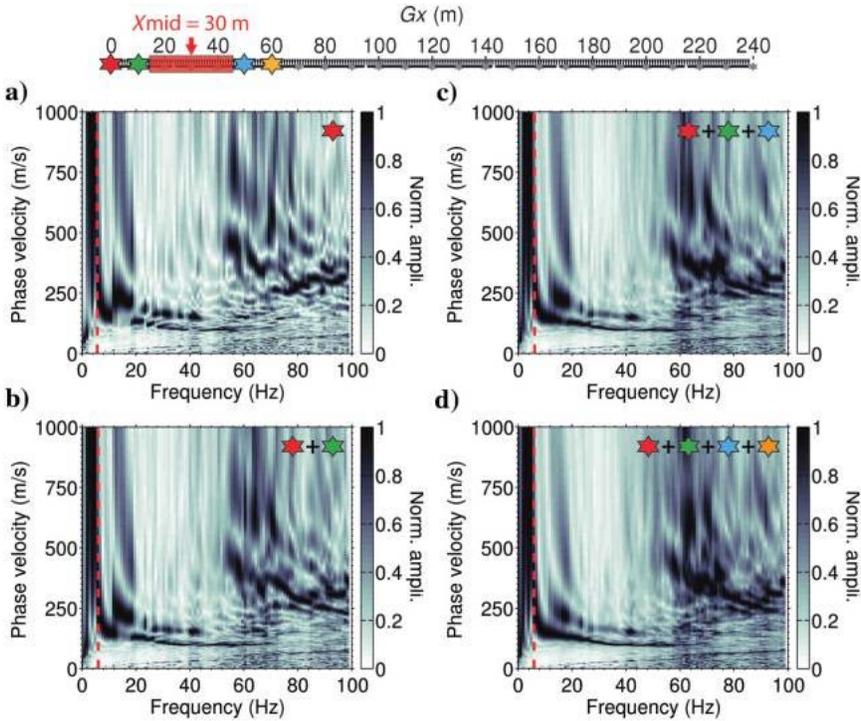
Figure 6.8 *(a-d) Successive stacking of the single dispersion images represented in Figure 6.7-a–d. From Pasquet and Bodet (2017).*
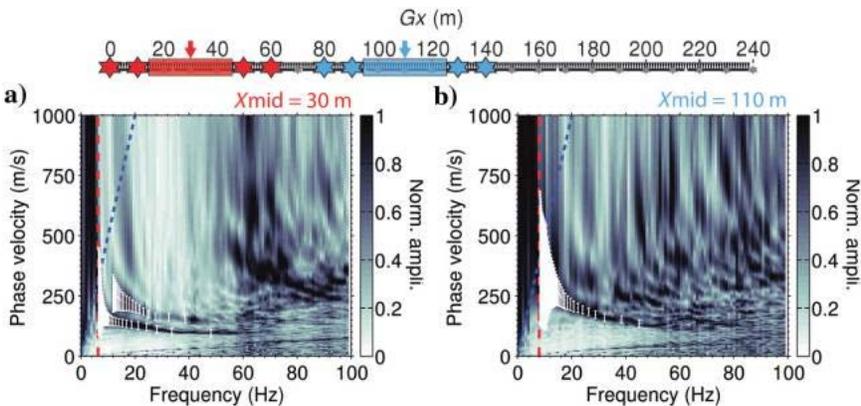

Figure 6.9 *Stacked dispersion images extracted at (a) Xmid = 30 m and (b) Xmid = 110 m with picked dispersion curves (white error bars) of the fundamental (0) and first higher (1) modes. The uncertainty range is defined according to the workflow described in O'Neill (2003). Dispersion curves are limited to a frequency defined with a spectral amplitude threshold of 2.5% (dashed red line), or up to a wavelength of 50 m (dashed blue line). From Pasquet and Bodet (2017).*

157

Adjacent dispersion images were displayed during picking to follow the lateral evolution of different modes and to avoid mode misidentification. The fundamental mode was clearly identified all along the line, whereas the first higher mode was only partially shown, as seen in Figure 6.10.
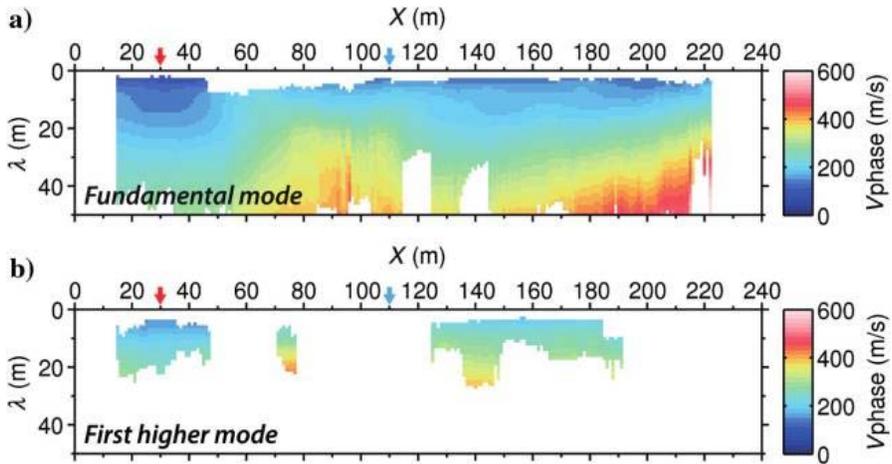

Figure 6.10 *Pseudo-sections of SW phase velocity picked for (a) the fundamental and (b) first higher modes along the line after dispersion stacking, represented as a function of the wavelength λ and the spread mid-point position. From Pasquet and Bodet (2017).*

A model with vertical velocity variation below each extraction window was assumed, therefore, the initial model chosen for the inversion is a one-dimensional stack of 10 homogeneous elastic layers based on a P-wave velocity model and geological information. A neighborhood algorithm (NA) without lateral constraints performs the inversion of the dispersion curves. The results for Xmid = 30 m and Xmid = 110 m are displayed in Figure 6.11.
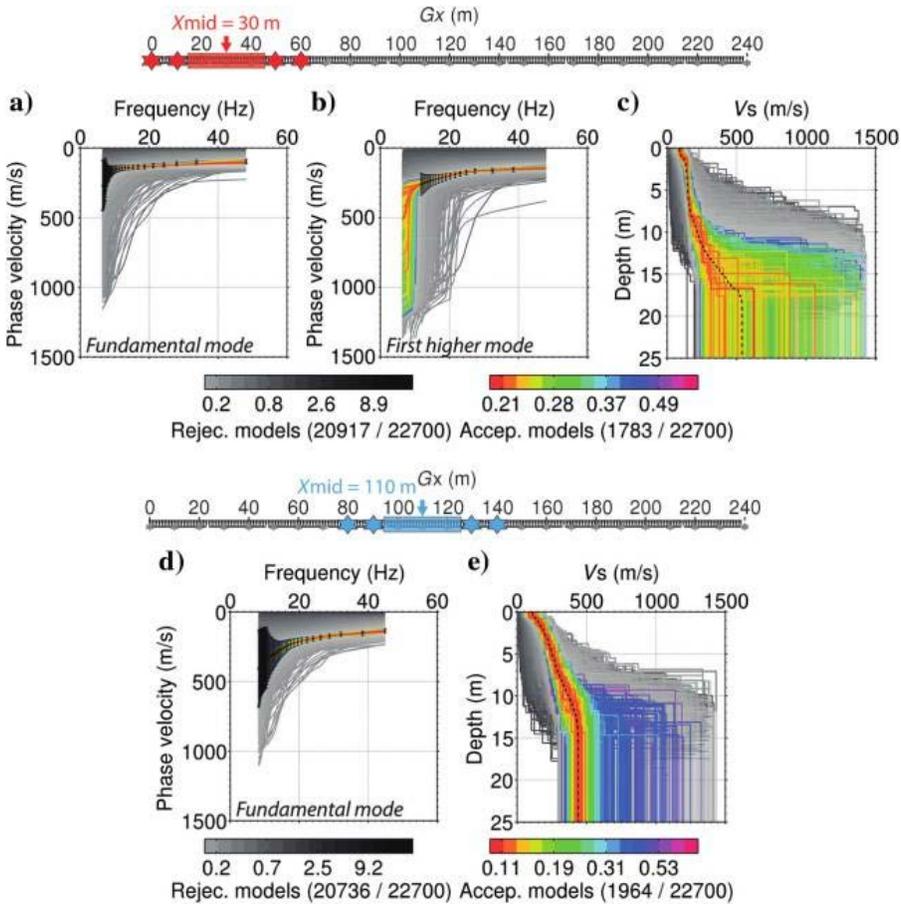
Figure 6.11 *Results of 1D NA inversions of dispersion data (black error bars) at Xmid = 30 m ([a] fundamental and [b] first higher modes) and Xmid = 110 m ([d] fundamental mode). Resulting VS models are represented for (c) Xmid = 30 m and (e) Xmid = 110 m, along with a misfit-weighted velocity structure (dashed black lines) built from the average parameters of all accepted models. Calculated dispersion and corresponding models are represented with misfit-based color and gray scales for accepted and rejected models, respectively. From Pasquet and Bodet (2017).*

After each 1D inversion, models fitting the observed data within the uncertainty were selected. For each extraction window model, a misfit-weighted model was built averaging all accepted models. Once this model had been constructed, its acceptability was evaluated by calculating the theoretical dispersion curves (Figure 6.12).
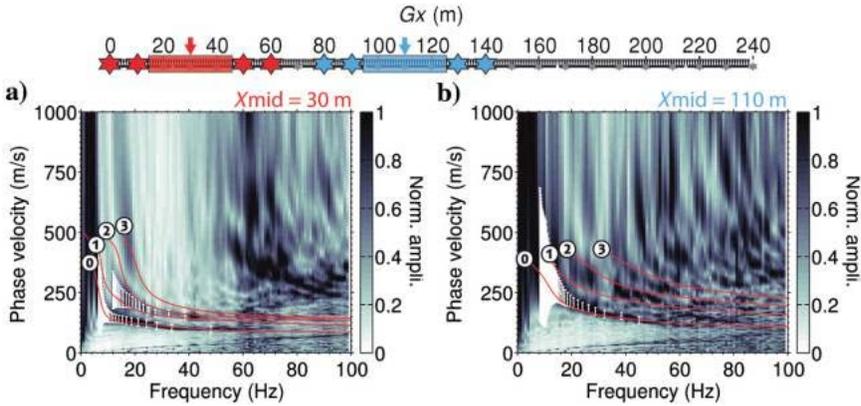
Figure 6.12 *Stacked dispersion images extracted at (a) Xmid = 30 m and (b) Xmid = 110 m with picked (white error bars) and calculated (solid red lines) dispersion curves represented for the fundamental (0), the first (1), second (2), and third (3) higher modes. From Pasquet and Bodet (2017).*

The study of the fitting parameters, for each 1D model provided by the inversion algorithm along the acquisition line, confirmed the good quality of this model. Then, the investigation depth was evaluated for each Xmid position and finally the pseudo-2D section of the S-wave velocity was built with each 1D S-wave velocity model. The final results are shown in Figure 6.13.
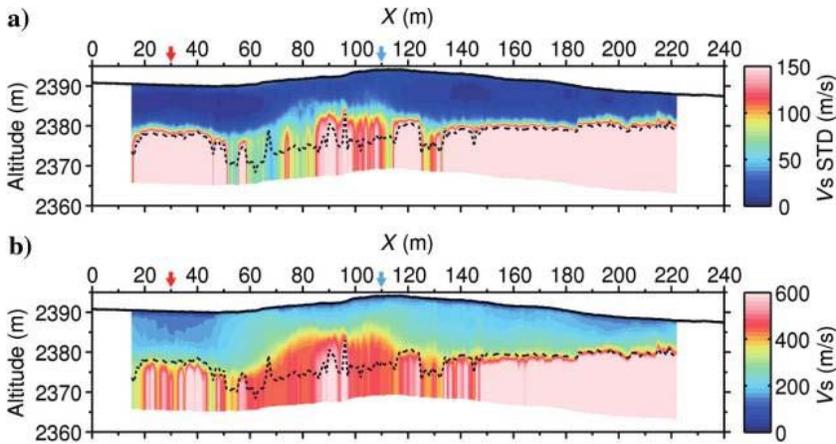

Figure 6.13 *(a) Pseudo-2D section of S-wave velocity standard deviation computed from accepted models at each Xmid position along the line. (b) Pseudo-2D section of average S-wave velocity model computed from accepted models at each Xmid position along the line. The dashed black line corresponds to the depth of investigation estimated with an S-wave velocity model standard deviation threshold of 150 m/s. The topography extracted from airborne LiDAR data is represented with a solid black line. From Pasquet and Bodet (2017).*

The S-wave velocity model is characterized by velocities ranging between 50 and 600 m/s, with higher shallow velocity below the heat-flow anomaly observed between 50 and 120 m. Although the S-wave velocity model has a lower investigation depth than the VP model, it provides more information regarding the lateral variations of the velocities of shallow layers due to the intrinsic smoothing of tomographic inversion and the substantial horizontal component of P-wave travel paths.

SWIP also calculates Poisson's ratio, if P-wave velocity is available. The results, as shown in Figure 6.14, reveal values in the range of 0.3–0.5, typical of non-saturated and saturated media, respectively. For most of the subsurface, Poisson's ratio values are between 0.45 and 0.5 indicating high water content, except in the highest part of the hill observed at depths below the degassing area visible at the surface, which presents a low Poisson's ratio.
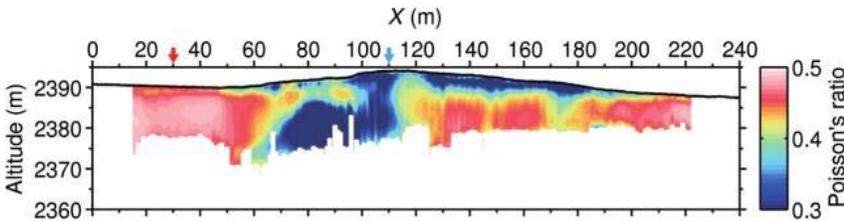

Figure 6.14 *Poisson's ratio computed from P-wave velocity provided by tomography and S-wave velocity from surface wave dispersion inversion and masked below the depth of investigation estimated from S-wave velocity standard deviation. The topography extracted from airborne LiDAR data is represented with a solid black line. From Pasquet and Bodet (2017).*

Finally, this example indicates that the estimated Poisson's ratio is a valuable parameter to clearly highlight gas pathways in the subsurface consistent with degassing observed at the surface.

6.3   Conclusion

This chapter, which describes the handling of different types of waves present within the same dataset, underlines some of the advantages of hybrid seismic imaging strategies to provide efficient, accurate and reliable subsurface models, in terms of geometry and mechanical properties.

In the first field example, the hybrid seismic imaging tool showed that seismic data derived from traditional refraction acquisition is valuable for obtaining information about the reflectivity for targets located in the near and/or very near surface. Based on a three-step procedure, the processing of refraction and reflection waves provided two sections, which after gathering produced an extended time reflectivity section starting from the surface.

The second example describes the use of hybrid seismic refracted and surface waves. The processing of surface waves, extracted from a seismic survey, was performed in the f-k domain with SWIP, an open-source MATLAB-based package. The inversion of the dispersion curves produced pseudo 2D models of S-wave velocity with an estimated depth of investigation of around 10 m. A P-wave velocity model was extracted from the refraction arrivals by a tomography algorithm. The Poisson's ratio was estimated from this information. The distribution of this parameter, more particularly its contrasts, clearly highlights gas pathways in the subsurface consistent with degassing observed at the surface.

The good results obtained in the case studies reveal that it is possible to obtain complementary information from the combination of different wave types from the same seismic survey. Thus, these hybrid seismic methods open up new perspectives for more applications.

References

Hagedoorn G.J., 1959, The Plus–Minus method of interpreting seismic refraction sections, *Geophysical Prospecting*, 7, 158-182.

Mendes M., Mari J.L., Hayet M., 2014, Imaging geological structures up to the acquisition surface using a hybrid refraction-reflection seismic method, *Oil & Gas Science Technology*, 69 (2), 351-361, http://dx.doi.org/10.2516/ogst/2012095.

Pasquet S., Bodet, L., 2017, SWIP: An integrated workflow for surface-wave dispersion inversion and profiling, *Geophysics*, 82 (6), WB47-WB61.